

## PROGRESS IN LASER FUSION

## Exploding Pusher Experiments on ZETA

An extensive series of implosion experiments utilizing DT filled glass microballoon targets with thin walls ( $0.6 - 1.4 \mu\text{m}$ ) has been carried out on the ZETA laser system during 1979. The symmetrical illumination provided by the 6 ZETA beams has produced impressive results in terms of implosion symmetry and neutron yield for these exploding pusher implosions. A neutron yield of  $1.5 \times 10^9$  was obtained for 1.67 TW of laser power (on target) in a 72 psec pulse, a record yield for this power level. Some of the important results of these experiments will be reviewed in this section.

Figure 5 is an example of an x-ray image (2-3 keV x-ray energy) showing the implosion symmetry routinely obtained. The diameter of the DT fill is typically reduced by a factor of 3-4 during these implosions. This observation, together with the initial DT density of  $\sim 4 \text{ mg/cm}^3$ , clearly shows that exploding pusher implosions compress DT to roughly liquid density ( $0.2 \text{ g/cm}^3$ ).

Neutron yields from a number of exploding pusher implosions are shown as a function of specific absorbed energy in Figure 6. For all these experiments, the ZETA beams were focused about 2 radii behind the target center, which results in symmetry similar to Figure 5. The attainment of yields greater than  $10^9$  for less than 2 TW of laser power

is attributed to the high degree of implosion uniformity obtained with the ZETA laser system.

**EXPLODING PUSHER IMPLOSION  
DT Compressed to ~Liquid Density**

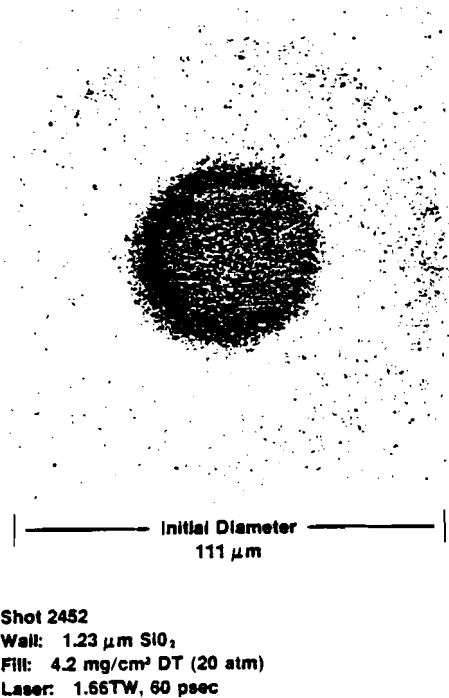


Figure 5 X-ray image of ZETA implosion

The solid line in Figure 6 was obtained by fitting the data with a very simple model, which assumes that the neutron yield can be considered only a function of DT ion temperature for these experiments, e.g., the slow dependence of compression on specific absorbed energy is ignored. The DT ion temperature,  $T_i$ , is taken as proportional to the specific absorbed energy,  $\epsilon$ . The neutron yield  $Y \sim n_D n_T V \tau \langle \sigma v \rangle$ , where the disassembly time  $\tau$  is proportional to the (ion sound speed)<sup>-1</sup> or to  $T_i^{-1/2}$ , and where the velocity averaged DT reaction cross section  $\langle \sigma v \rangle \sim T_i^{-2/3} \exp(-19/T_i^{1/3})$  with  $T_i$  in keV. Thus  $Y = A \epsilon^{-7/6} \exp(-B/\epsilon^{1/3})$ .

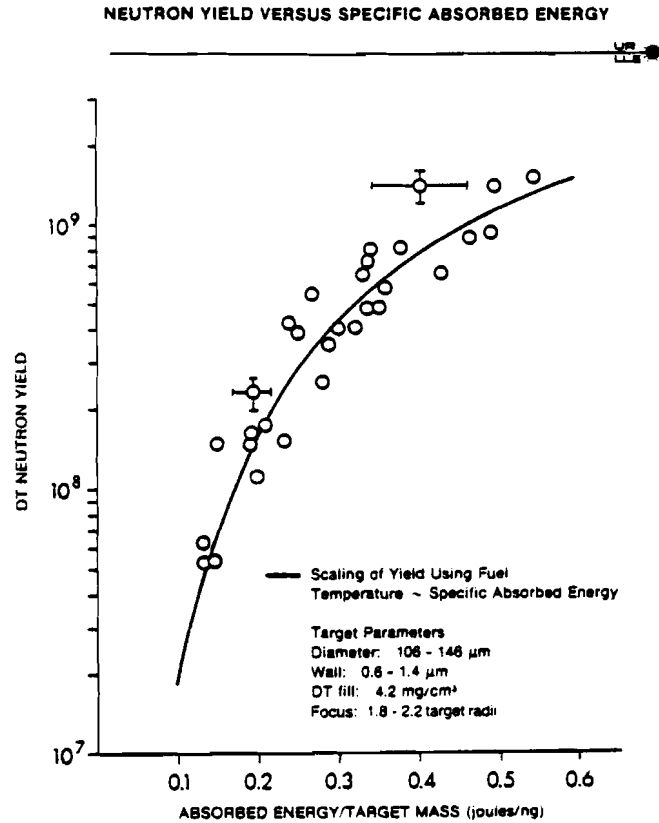


Figure 6

The constants A and B are chosen to give the best curve fit through the data. In the model the rolloff in the yield curve as  $\epsilon$  increases is chiefly a result of the temperature dependence of  $\langle\sigma v\rangle$ . A major challenge for the future will be to move above this scaling by increasing the compressed DT density.

The 1-D Lagrangian hydrodynamic implosion code LILAC (including multi-group suprathreshold electron transport) has been utilized to simulate these experiments. The computations generally support the features of the simple model above and the computed yield is quite close to experiment, generally higher than experiment by a factor of

1-2. Since these computations are performed with no artificial reduction in the yield calculation to account for implosion asymmetries, for example, the reasonable agreement is another indication of good spherical symmetry for these experiments.

An examination of the effect of beam focusing on neutron yield is shown in Figure 7. In this figure the measured/calculated neutron yield is plotted versus the beam focal position. The calculated yield was taken from the simple scaling model of Figure 6 and is used to remove the dependence on specific absorbed energy. For beam focusing near 2 radii, the yield ratio scatters about 1.0, since the scaling

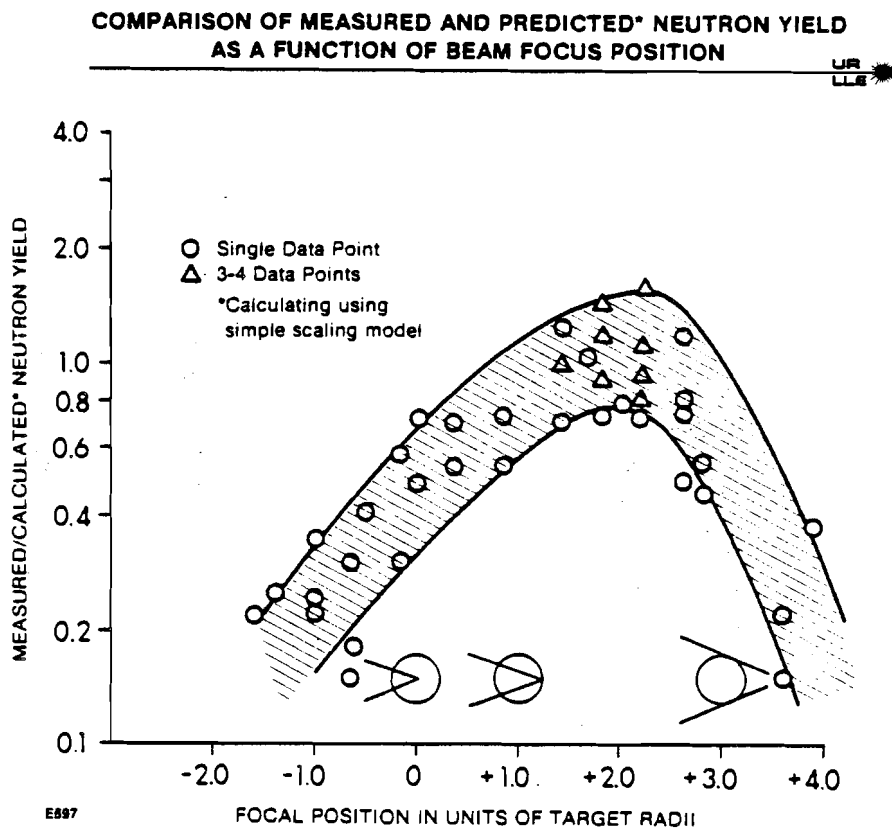


Figure 7

model was normalized at that focal position. This focusing position is optimum for neutron yield. As the focal position is shifted to surface focus (focal position of -1 in Figure 7) the neutron yield drops dramatically relative to the scaling model. The x-ray imaging results<sup>1</sup> also show a steady increase in structure as the focal position is shifted from +2 to -1, implying that only sections of the target are being imploded at high velocity when the beams are focused on the surface. The decrease in neutron yield would appear to result from the decrease in implosion symmetry.<sup>2</sup> The decrease in relative yield for focal positions beyond +2 is not clearly understood.

Alpha particle and proton energy spectra have also been measured for these experiments with a quadrupole time-of-flight detector. From the width of the alpha spectrum, DT ion temperatures have been measured from 2 to 6 keV and to be approximately proportional to the specific absorbed energy, as assumed in the simple neutron scaling model above. The mean alpha energy can be expected to be downshifted during passage through the glass tamper by an amount which depends on the temperature and  $\rho R$  of the tamper. Energy downshifts have been observed, but for high specific absorbed energy implosions, alpha energy upshifts are seen instead<sup>3</sup> (Figure 8). This is interpreted as acceleration of the alpha particles as they traverse an electrostatic potential generated by suprathermal electrons. Such a potential would be expected from high energy electrons which escape the target entirely and from quasi-neutral and sheath potentials in the corona. For the data of Figure 8, a minimum estimate for the potential of up to 215 kV can be deduced from the magnitude of the energy upshift

**SCALING OF ALPHA PARTICLE MEAN  
ENERGY WITH SPECIFIC ABSORBED ENERGY**

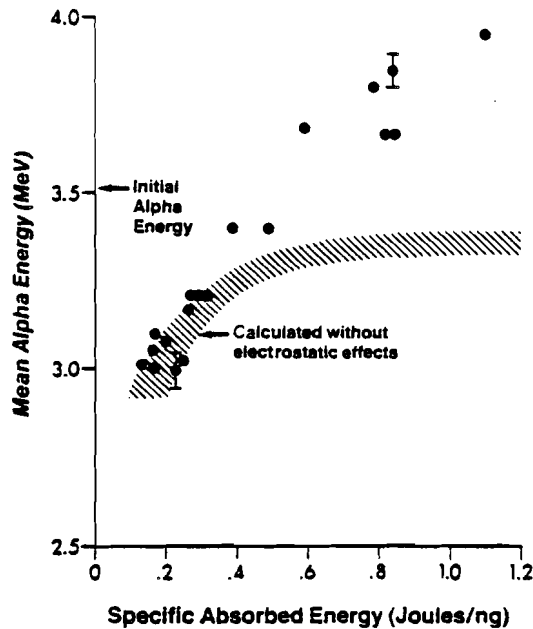


Figure 8

alone. By comparing with LILAC calculations of the expected alpha spectrum without electrostatic effects (hatched region, Figure 8), time averaged potentials up to 300 kV can be inferred.

In order to clarify the specific absorbed energy dependence of the alpha energy upshift, Figure 9 gives the LILAC result for the time history of the cumulative alpha particle production relative to the laser pulse for low and high specific absorbed energy shots. For the low specific absorbed energy shot 1917 the implosion velocity is relatively low and the alpha particles are produced essentially after the laser pulse. For shot 1917 and similar shots, alpha particle energy downshifts are observed. For shot 1801, with higher specific absorbed energy, the shorter implosion time results in alpha particle

## ALPHA PRODUCTION TIME HISTORY CALCULATION

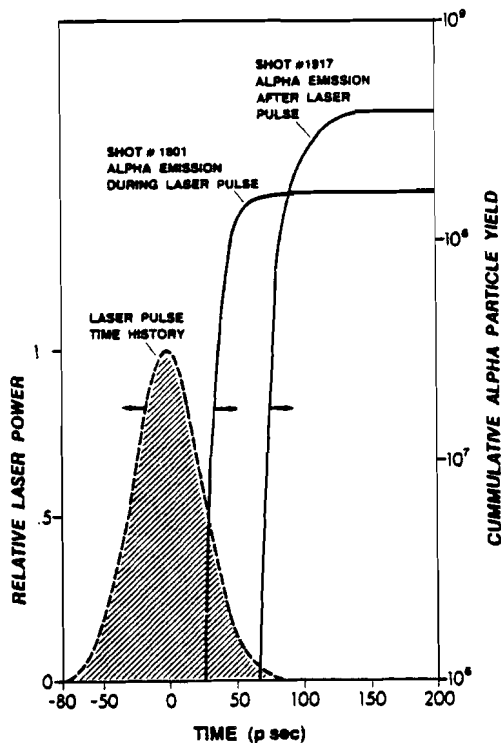


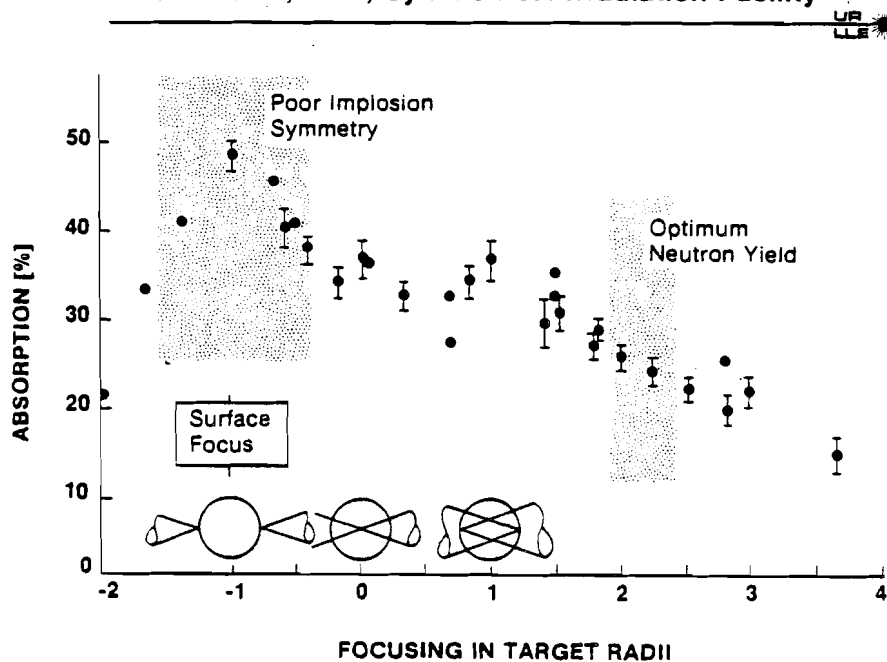
Figure 9 Alpha production time history relative to the laser pulse calculated by the code LILAC: high specific absorbed energy (0.79 J/ng) for shot 1801; low specific absorbed energy (0.26 J/ng) for shot 1917

production during the laser pulse. For shot 1801 and similar shots, alpha particle energy upshifts are observed. This is consistent with an electrostatic potential which decays rapidly after the laser pulse and hence after cessation of energetic electron production. Rapid potential decay may occur through neutralizing currents from the target stalk or through cooling of the energetic electrons by expansion and fast ion production. It should be noted that for cases with alpha energy upshifts, the time varying nature of the electrostatic potential can also broaden the spectrum substantially, thereby complicating DT ion temperature determinations for such cases.

Finally, the fractional absorption of incident  $1.054 \mu\text{m}$  laser radiation onto targets in 50-70 psec pulses has been measured with an array of 12 differential plasma calorimeters. The results for absorption versus beam focal position are shown in Figure 10. The absorption fraction is typically 30% at a focal position of 2 radii behind target center, the optimum position for neutron yield. The peak intensity for this case is about  $5 \times 10^{15} \text{ W/cm}^2$ . Near surface focus, the absorption fraction rises to 50%, while implosion symmetry and yield are substantially degraded. For surface focus, the peak intensity is  $\geq 10^{17} \text{ W/cm}^2$ .

In an attempt to understand the absorption mechanism in the varying focusing regions, we have employed an axially symmetric ray

**ABSORPTION AS FUNCTION OF FOCUSING**  
**Zeta 6-Beam, 3TW, Symmetrical Irradiation Facility**

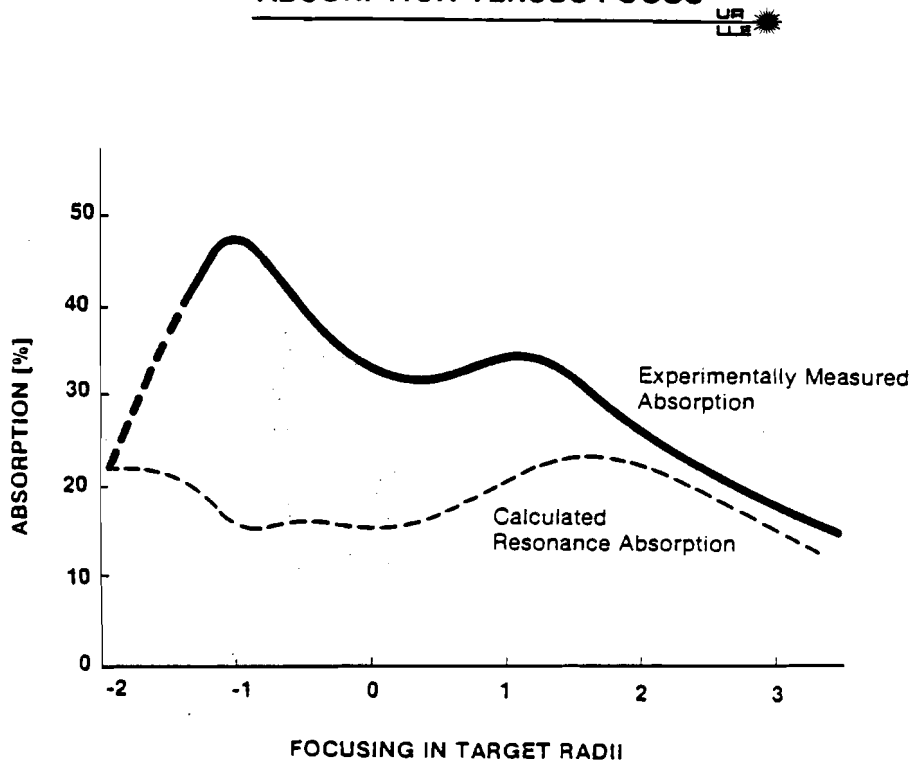


E708

Figure 10

tracing code to compute resonance absorption for circularly polarized beams taking into account profile steepening and incident angle variations across the beam profile. A comparison of the calculated and experimental absorption is shown in Figure 11. We observe that this resonance absorption model can account for the experimental data beyond a focal position of 2 target radii. On the other hand, there is substantial disagreement for other focusing conditions where the intensity increases to the  $10^{16} - 10^{17}$  W/cm<sup>2</sup> range, and where strong spatial modulation of the incident intensity exists because of low irradiance conditions between the beams. It can only be speculated at this point that effects such as deformation of the critical density surface may be essential for calculation of absorption in this regime.

### ABSORPTION VERSUS FOCUS



E710  
Figure 11

1. E. I. Thorsos, T. C. Bristow, J. A. Delettrez, J.M. Soures, and J. E. Rizzo, Appl. Phys. Lett. 35, 598 (1979).
2. It is probable that a higher percentage of the absorbed energy appears in fast ions as the intensity increases near surface focus. This will also have the effect of decreasing the yield.
3. Y. Gazit, J. Delettrez, T. C. Bristow, A. Entenberg, and J. Soures, Phys. Rev. Lett. 43, 1943 (1979).

### Intermediate Density Experiments on ZETA: DT Fill

In order to obtain compressed DT densities higher than liquid density, a number of experiments have been performed with DT filled plastic coated glass microballoon targets with plastic thicknesses up to 10  $\mu\text{m}$ . Up to 150 J of laser energy was applied in 50-80 psec pulses to targets with diameters ranging from 80-130  $\mu\text{m}$ . Compressed DT densities up to 10x liquid density have been inferred with x-ray imaging for these implosion experiments.

X-ray pinhole camera imaging has shown in exploding pusher implosions that the ZETA laser system is capable of producing symmetric implosions when the beams are focused several radii behind the target. This observation has been extended to higher compression implosions (up to a compression of  $\sim 500$ ) with thick shell targets. To clearly resolve the "inner ring," that is, the inside of the  $\text{SiO}_2$  tamper location, requires imaging with relatively hard x-rays to avoid opacity effects from the surrounding cold tamper. The hardest x-ray channel in the x-ray pinhole camera is in the 3-4 keV range. This x-ray energy coupled with 3-4  $\mu\text{m}$  diameter pinholes yields quite good resolution ( $\sim 4 \mu\text{m}$ ) as shown in Figure 12 (inset). The densitometer scan shows for this implosion that the  $\text{SiO}_2$  stagnated with an inner diameter of 20  $\mu\text{m}$ . The DT inside radiates negligibly because of its lower Z. Assuming the fill gas is entirely trapped, this diameter immediately yields a compressed density. There are pitfalls associated with this method, however. To be convincing, the following conditions should be met: (1) the focusing of the laser beams should be optimized for symmetric

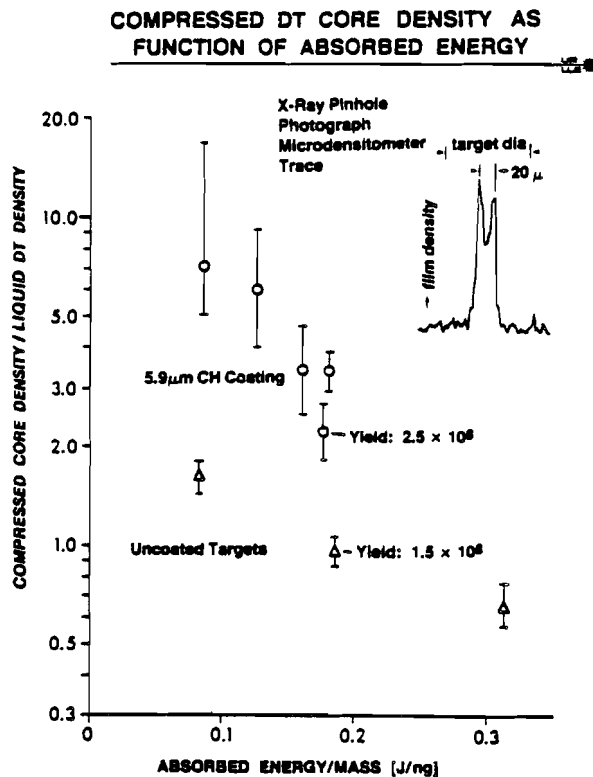
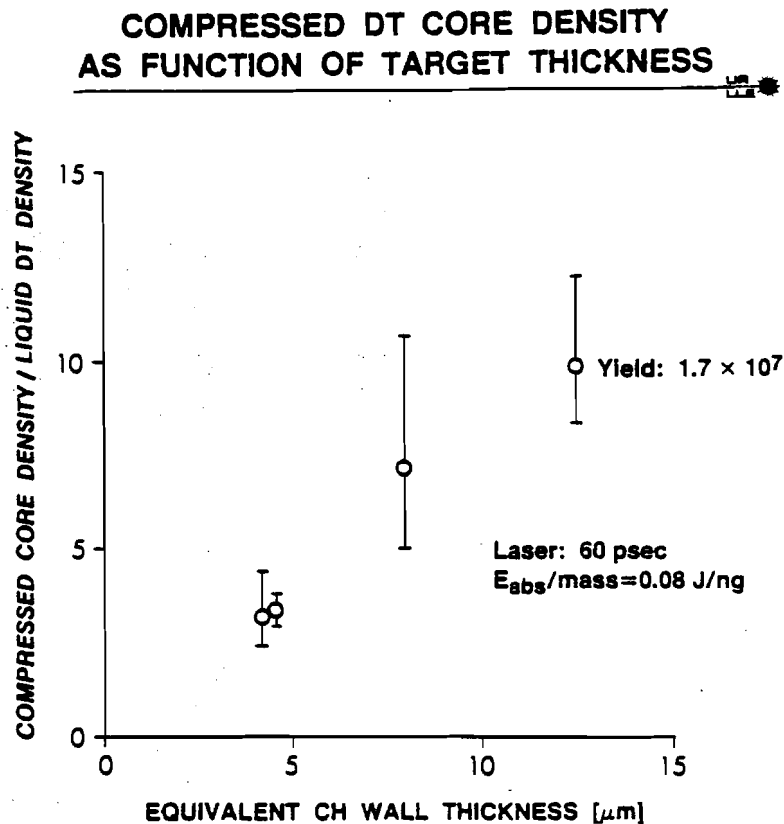


Figure 12

implosions; (2) the inner ring should be nearly spherically symmetric, as observed with more than one view of the implosion, and (3) the compression results should form a smooth and consistent trend to higher densities as the wall thickness is increased. All of these conditions have been met in our experiments; in particular, two pinhole cameras have been used to check on symmetry.

Results for compressed DT densities from x-ray imaging for two kinds of targets are shown in Figure 12. The three triangular points are for relatively thin targets, in this case uncoated glass microballoons filled with  $4.2 \text{ mg/cm}^3$  DT. We would expect these targets to behave in typical exploding pusher fashion yielding compressed DT

densities near liquid density, which they do. The other points are for thicker shell targets: 6  $\mu\text{m}$  of CH on top of 0.8  $\mu\text{m}$  of  $\text{SiO}_2$  with a total target diameter of about 90  $\mu\text{m}$ . These targets are filled with about 10  $\text{mg}/\text{cm}^3$  of DT. The increased shell mass for these targets leads to increased compressed density as would be expected from simple exploding pusher scaling arguments. The rise in compressed density for reduced specific absorbed energy would be expected qualitatively from (1) lower fuel preheat by suprathreshold electrons (at lower incident intensity) and from (2) less shock heating in the fuel from the lower implosion velocity resulting in a lower fuel adiabat. This result suggests that in comparing compressed density as a function of target wall thickness, it may be advantageous to hold the specific absorbed energy constant. Figure 13 shows that as the wall thickness is increased holding the



E726

Figure 13

specific absorbed energy constant, the compressed DT density is also increased up to 10x liquid density. The equivalent CH wall thickness is obtained by replacing the  $\text{SiO}_2$  by an amount of CH of equal mass.

Implosion times were also obtained for these experiments with an x-ray streak camera. Analysis of this data and overall comparison with LILAC simulations are presently underway.

## Intermediate Density Experiments on ZETA: Ar Fill

Argon filled plastic coated glass microballoon targets have also been imploded with short, high intensity, laser pulses: 100 - 150 J in ~ 50 psec laser pulses. The role of the Argon was two-fold: (1) to partly mitigate the effect of preheat through radiational cooling and thereby enable a higher compression, and (2) to serve as a direct diagnostic of the compressed density ( $\rho$ ) and the quality of confinement ( $\rho R$ ). The measurement of the density (using x-ray line Stark broadening) allows an experimental verification of whether a given predicted compression (with any fill) can actually be achieved or whether it is prevented by the lack of perfect spherical symmetry, instability or shell-fill mixing. The various x-ray lines utilized for density determinations are predicted to have different widths and very different shapes, and therefore a consistent agreement with this large number of observables constitutes a highly reliable determination of the compression. Densities in the range of 4-6 g/cm<sup>3</sup> ( $n_e = 1.0 - 1.5 \times 10^{24} \text{ cm}^{-3}$ ) at temperatures ~ 1 keV were deduced from the Stark profiles of various Ar<sup>+16</sup>, Ar<sup>+17</sup> x-ray lines.<sup>1</sup> These densities are achieved partly due to radiational cooling of the high-Z fill gas and show that symmetric illumination can result in high volume compression (> 1000).

In order to employ the observed lines for  $\rho$  and  $\rho R$  determinations, an estimate is needed for the temperature during the time of emission, and the opacity (self-absorption of the lines). Fortunately, the line profiles are not very sensitive to temperature, especially for helium-like ions. For high density shots  $T_e$  was found to be about 0.8

keV using various line intensity ratios. It can be shown on rather general grounds for these experiments that the optical depth of the  $\text{Ar}^{+17}$  Lyman- $\beta$  line will be near unity or less, and therefore the line profile will be only modestly affected by opacity. In addition, the Lyman- $\beta$  profile has a double peak structure, and the peak separation is relatively insensitive to opacity (compared to the width, for example). The Lyman- $\beta$  peak separation is therefore very useful in obtaining a first estimate of density. An example of a density determination is shown in Figure 14 for shot 3231. The Lyman- $\beta$  line was fitted with a profile for an electron density  $n_e = (1.5 \pm 0.4) \times 10^{24} \text{ cm}^{-3}$  (which corresponds to  $\rho \sim 6 \text{ g/cm}^3$ ) without any opacity correction; a small opacity correction would further improve agreement with experiment. Analysis of other lines for this shot gives consistent results.

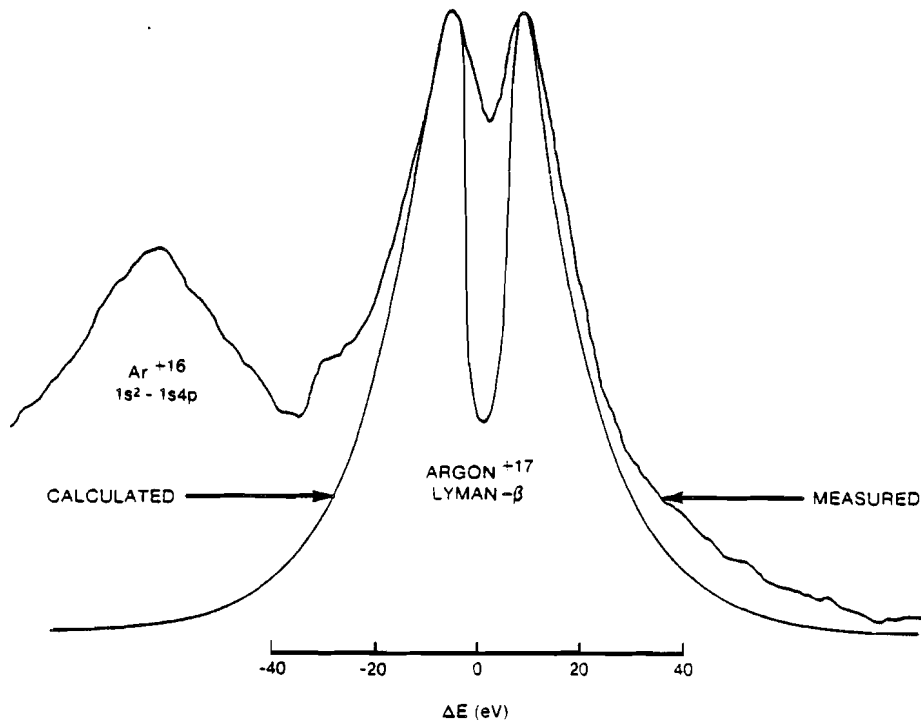


Figure 14 Argon Lyman- $\beta$  line from shot 3231 with fitted profile. The density determination was  $n_e = (1.5 \pm 0.4) \times 10^{24} \text{ cm}^{-3}$  or  $\rho \sim 6 \text{ g/cm}^3$ .

Some of the more dramatic profile changes with density are shown by the spectral profile of the  $1s^2 - 1s3p$  line of  $\text{Ar}^{+16}$  and its forbidden neighbor  $1s^2 - 1s3d$ . Figure 15 shows a comparison of the profile of these lines for a high density shot (2495) and for a lower density shot (2416). At high plasma densities the quadratic Stark effect should cause the forbidden line to increase in intensity and the two lines to move apart and broaden. All these features are clearly seen in Figure 15. Stark profile fitting (Figure 16) yields an electron density  $n_e = (0.96 \pm 0.24) \times 10^{24} \text{ cm}^{-3}$  ( $\rho \sim 3.8 \text{ g/cm}^3$ ).

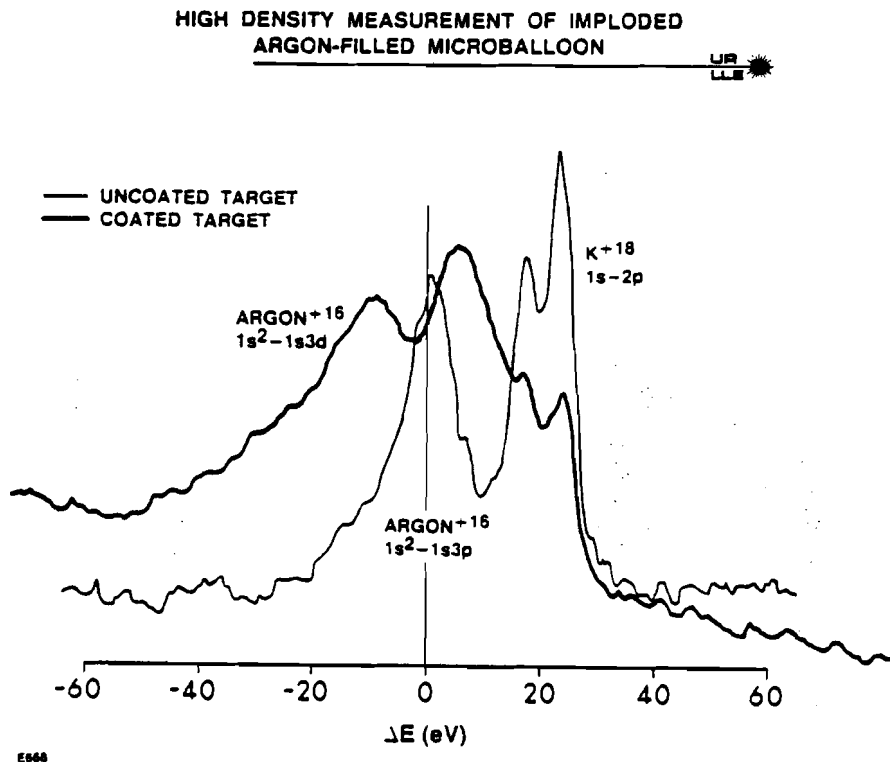


Figure 15 Argon lines from shot 2495 (plastic coated target) and from shot 2416 (uncoated target)

## HIGH DENSITY MEASUREMENT OF IMPLoded ARGON-FILLED MICROBALLOON

UCLA  
LLE 

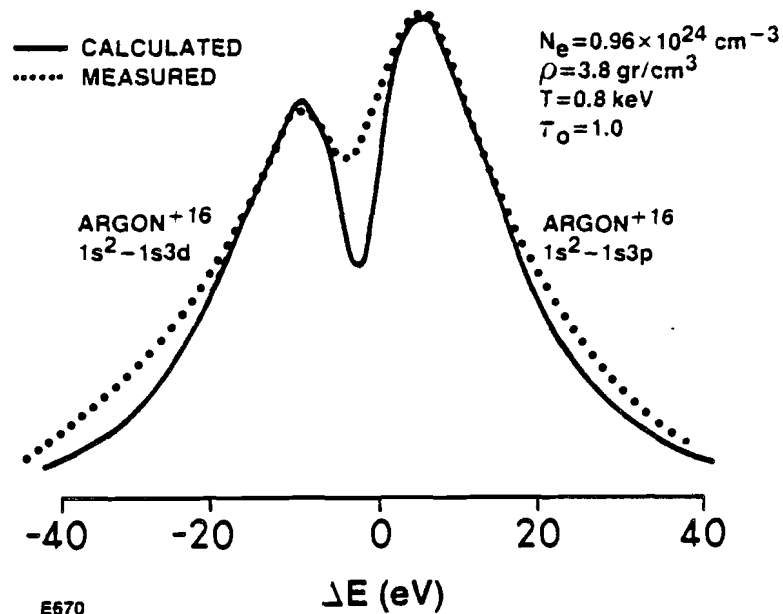
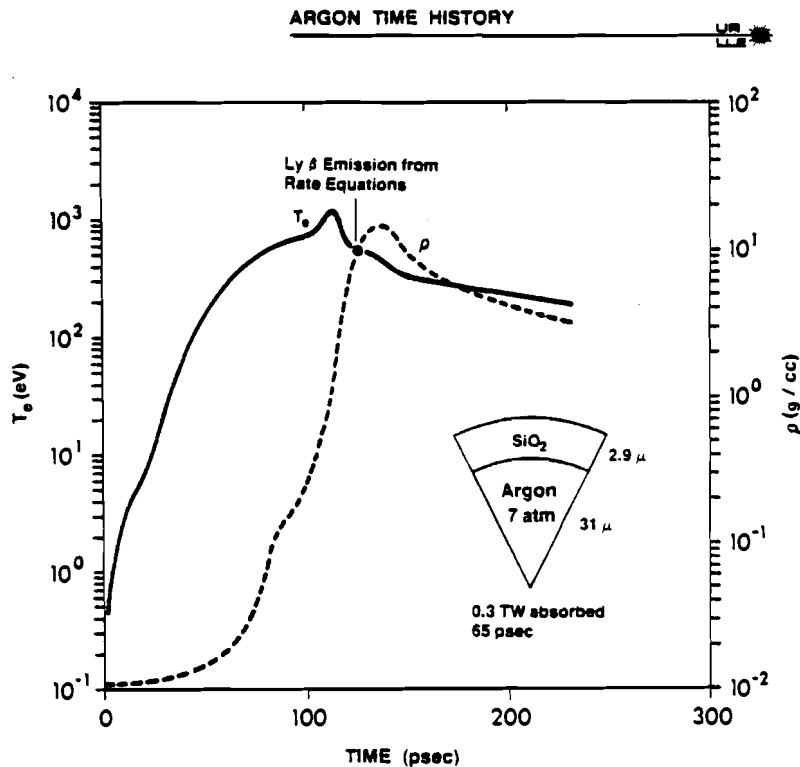


Figure 16 Density determination by fitting the observed lines for shot 2495 in Figure 15 with a computed Stark profile

Analysis of Ar line profiles has yielded convincing evidence of compressed Argon densities in the range of 4-6 g/cm<sup>3</sup> ( $n_e = 1.0 - 1.5 \times 10^{24} \text{ cm}^{-3}$ ). Analysis of the optically thick Ar<sup>+17</sup> Lyman- $\alpha$  line also yields information on the Argon  $\rho R$  at time of emission: for example, for shot 3231, we find  $\rho R = 1.5 \pm 0.5 \times 10^{-3} \text{ g/cm}^2$ . The  $\rho$  and  $\rho R$  determinations are consistent with each other if the Ar is assumed to be totally confined inside the tamping shell. We therefore have additional evidence that for the symmetrical illumination of the ZETA laser system, the implosion symmetry is good and significant shell breakup does not occur (up to the time of line emission).

The relatively high density obtained with these Argon filled targets is due in part to radiational cooling of the Argon. This can be seen from LILAC simulations for these experiments. Figure 17 shows the average temperature and density time histories in the Argon for a thick shell Argon filled target. The cooling immediately following the temperature maximum is due largely to Argon radiational cooling, and significantly increased densities result. The simulations are done with a rate equation treatment for the Argon ionization states, and show that the line emission occurs in a short ( $\sim 10$  psec) time interval around the time indicated. This explains why the experimental profiles can be so well fit by a theoretical profile for a single density. The Argon line profiles produced in the simulation also match well with experimental profiles.



TC541

Figure 17 Average temperature and density time histories calculated by LILAC

1. B. Yaakobi, S. Skupsky, R. L. McCrory, C. F. Hooper, Jr.,  
H. Deckman, P. Bourke, and J. M. Soures, "Symmetric Laser  
Compression of Argon-Filled Shells to Densities of 4-6 g/cm<sup>3</sup>,"  
submitted to Physical Review Letters.

### Diagnostic Development: Alpha Particle Imaging

Successful fabrication of free standing gold zone plates of up to 8  $\mu\text{m}$  thickness has been accomplished. This has enabled the recording of alpha-particle coded images on a few high yield exploding pusher implosions on ZETA. First order reconstructed images have been obtained in two cases, one corresponding to symmetrical focusing and implosion, and the other to center focusing conditions. Figure 18 shows isodensity contours obtained from the reconstruction for the two shots. They correspond to contours of constant alpha-particle time-integrated intensity, which displays a peak in the center for both shots. The targets had diameters of 112  $\mu\text{m}$ , wall thicknesses of 0.7  $\mu\text{m}$ , and were filled with 20 atm of DT. For Figure 18a, the beams were focused for near symmetrical illumination and the alpha-particle contours are roughly circular extending over a region about 30  $\mu\text{m}$  in diameter. The yield for this shot was  $1.1 \times 10^9$  with 1.8 TW on target. For Figure 18b, the beams were focused on the center of the target, which resulted in significant structure in the x-ray image. Similarly, the alpha-particle contour plot shows evidence of the six ZETA beams. A reduced yield of  $4.7 \times 10^8$  was obtained with 2.05 TW on target. We have tentatively concluded that the outward extensions of the contours in Figure 18b are along the incident beam directions.

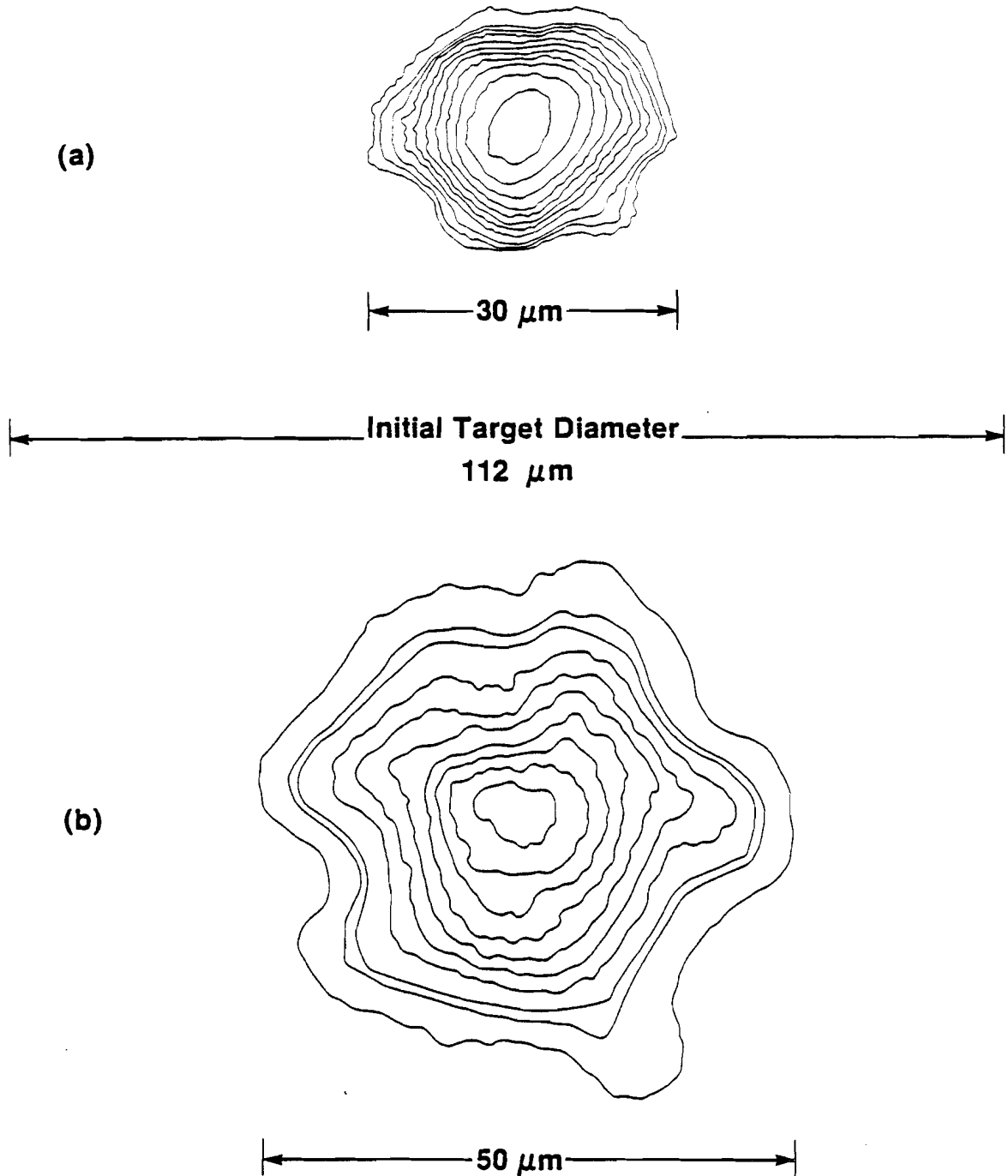


Figure 18 Contours of constant alpha-particle time-integrated intensity: (a) beams focused 1.4 radii beyond the target center for near symmetrical illumination; (b) beams focused at the target center